Acta Materialia 97 (2015) 124–130

Contents lists available at ScienceDirect

Acta Materialia

journal homepage: www.elsevier.com/locate/actamat

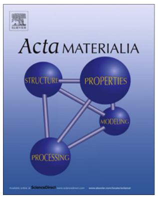

Influence of oxide volume fraction on abnormal growth of nanostructured ferritic steels during non-isothermal treatments: An *in situ* study

X. Boulnat[a,b,*], N. Sallez[c], M. Dadé[a], A. Borbély[e], J.-L. Béchade[a], Y. de Carlan[a], J. Malaplate[a], Y. Bréchet[c,d], F. de Geuser[c,d], A. Deschamps[c,d], P. Donnadieu[c,d], D. Fabrègue[b], M. Perez[b]

[a] *CEA, DEN, Service de Recherches Métallurgiques Appliquées, 91191 Gif-sur-Yvette, France*
[b] *Université de Lyon, INSA-Lyon, MATEIS UMR CNRS 5510, F69621 Villeurbanne, France*
[c] *Univ. Grenoble Alpes, SIMAP, F-38000 Grenoble, France*
[d] *CNRS, SIMAP, F-38000 Grenoble, France*
[e] *Ecole Nationale Supérieure des Mines, SMS-EMSE UMR CNRS 5307, F42023 Saint-Etienne, France*

ARTICLE INFO

Article history:
Received 11 March 2015
Revised 15 June 2015
Accepted 2 July 2015
Available online 12 July 2015

Keywords:
In situ X-ray diffraction
Abnormal growth
Recrystallization
Precipitation
Pinning

ABSTRACT

Nanostructured ferritic steels were mechanically alloyed with various contents of oxide-forming yttrium and titanium (0, 0.05, 0.3 and 1 wt%). The microstructure evolution of the milled powders during non-isothermal annealing treatments was studied using *in situ* synchrotron X-ray diffraction. Recrystallization and grain growth were quantified upon heating up to 1100 °C, which is the typical consolidation temperature for nanostructured ferritic steels. The temperature where abnormal grain growth occurs is observed to increase with the volume fraction of oxide nanoparticles. This demonstrates the interest of increasing the amount of alloying elements to limit the formation of the bi-modal grain microstructure. Using the nanoscale characterization of the precipitation state, the size of retained ultrafine grains (UFG) in the bimodal microstructure was found to be in agreement with the modified Zener theory demonstrating that the microstructure of ultrafine-grained steels can be tailored by the amount and size of second-phase particles.

1. Introduction

Oxide-dispersion strengthened (ODS) ferritic steels are developed for high-temperature applications due to their excellent creep properties. This key-property is achieved thanks to a fine microstructure reinforced by a very dense dispersion of nano-oxides. The processing route involves powder metallurgy where high-energy milling is followed by hot isostatic pressing [1–4], hot extrusion [5] or more recently by field-assisted sintering [6,7]. The original nanostructure obtained by mechanical alloying combined with the rapid precipitation during annealing causes undesirable behavior with respect to recrystallization, resulting in abnormal grain size distribution. Such heterogeneous microstructure contributes to the high anisotropy of the extruded microstructure which results in low transverse creep strength [1,5]. Abnormal grain growth in ODS steels is frequently related to nanoparticles Zener pinning [8,9] and often extended to corner pinning on multiple junctions [10,11]. Appearance of abnormal grains is a key-issue that does not only affect ODS materials but largely influences the properties of nanostructured metallic materials. Indeed, tailoring the nanosized-to-coarse-grains ratio is an efficient way to achieve a good compromise between mechanical strength and ductility [12,13]. Yet, the microstructural instabilities occurring during hot processing of nanostructured metallic materials such as recovery, recrystallization and grain growth remain only partially explored since they can be concomitant. Hence, this has not been quantified in a time-resolved manner yet. Indeed, this requires to perform an *in situ* characterization of the physical parameters that can give insight both into the stored energy (density of crystalline defects) and the microstructural changes (grain size) occurring during hot processing. X-ray diffraction (XRD) can be very accurate to describe the dislocation structure and crystallite size of ultrafine grained material [14–19]. A specific *in situ* XRD analysis for abnormal grain growth was recently set up [20], and will be employed here.

---

* Corresponding author at: CEA, DEN, Service de Recherches Métallurgiques Appliquées, 91191 Gif-sur-Yvette, France.

E-mail addresses: xavier.boulnat@insa-lyon.fr, boulnat.xavier@gmail.com (X. Boulnat).

http://dx.doi.org/10.1016/j.actamat.2015.07.005
1359-6454/

In this work, a pre-alloyed ferritic powder of composition Fe–14Cr–1W (in wt%) was mechanically alloyed with an increasing content of yttrium and titanium. *In situ* XRD acquisition during non-isothermal heating up to the consolidation temperature of 1100 °C was used to determine the kinetics of microstructural evolution within the different powders, namely recovery, crystallite growth and the occurrence of heterogeneous (secondary) recrystallization. From an engineering point of view, the temperature at which abnormal grains appear is a key factor for optimizing the consolidation process and therefore was determined for each material.

Transmission Electron Microscopy combined with the orientation determination device referred to as Automatic Crystallographic Orientation Mapping (TEM–ACOM) was used to characterize the final grain microstructure. The nanoscale precipitation was also evaluated using Small Angle X-ray Scattering (SAXS). Classical Scanning Electron Microscopy (SEM) was then employed to complete the characterization at the grain scale. On the basis of the Zener pinning pressure theory, these results were used to address a law describing the influence of composition and precipitation on the microstructural behavior of nanostructured ferritic ODS steels.

2. Materials and methods

The base powder of high-chromium ferritic steel was produced by gas atomization by Aubert & Duval. The powder particles were spherical with a mean diameter of 70 µm. They were composed of an iron matrix with chromium (14.5 wt%), tungsten (1 wt%), manganese (0.3 wt%), and silicon (0.3 wt%). This powder was then milled with respectively 0, 0.05, 0.3 and 1 wt% of yttria (Y_2O_3) and titanium hydride (TiH_2) in a high-energy attritor for 10 h each in the same conditions (Table 1). The milling process was performed at a speed of 400 rounds per minute (rpm), under argon, for 10 h. The ball-to-powder weight ratio was around 15. Yttrium being added under the form of yttrium oxides (Y_2O_3), the oxygen content is therefore directly related to the yttrium content. However, in addition to this direct oxygen source, numerous studies showed that there is a second oxygen source, which is referred to as "excess oxygen" resulting from contamination during milling. The oxygen quantity brought by this second source is far from negligible [4]. The actual chemical compositions measured on each powder batch are given in Table 1.

Using a furnace dedicated to powder heating, the same anisothermal treatment simulating the consolidation process from room temperature up to 1100 °C was performed under vacuum on each powder.

X-ray diffraction (XRD) was used to study the microstructure evolution of the nanostructured powders during annealing. More specifically, X-ray diffractograms of the 4 major ferrite peaks were recorded separately with a last generation 2D detector XPAD S140 [21]. The obtained diffractograms were analyzed with a coupled modified Warren–Averbach and Williamson–Hall method, which is fully described in [20]. This method allows to accurately calculate the dislocation density and the crystallite size. Their contribution to peak broadening is given by:

$$\beta_{ODS}(t) = \frac{0.9}{D(t)} + \frac{\pi}{2} Re^2(t) b^2 \rho^{3/2}(t) K^2 \bar{C} \pm O(K^4 \overline{C^2})$$

where β_{ODS} is the full width at half maximum of a specific diffraction peak, K is the scattering vector defined by $K = 2\pi \sin(\theta)/\lambda$, D is the crystallite size, the dislocation density is expressed as ρ, Re is the outer cut-off radius of dislocations, b is the Burgers vector magnitude and $\bar{C}$ the contrast factor.

TEM–ACOM maps were acquired on a 200 keV Tecnai F20 ST (FEI) using a 1 nm nano-beam and a 2.75 nm step size. TEM–ACOM provides orientation maps very similar to the ones obtained by EBSD. TEM thin foils were prepared by Focus Ion Beam (FIB) directly from the annealed powder particles.

SAXS measurements were carried out on a laboratory rotating anode with a Mo target. Data was acquired using a 2D detector, and was available in a q-range of [0.02, 0.5] $Å^{-1}$. The mean radius of precipitates was estimated assuming a log-normal distribution for the precipitate size distribution, and the volume fraction was calculated assuming a composition of the oxides of $Y_2Ti_2O_7$ and by calibrating the beam intensity by the scattering of a sample of amorphous carbon. For the sake of the measurements efficiency, the as-milled powders were then canned and further consolidated by hot isostatic pressing (HIP) at 1100 °C for 2 h under 1900 bar.

Table 1
Content of yttrium and titanium measured for each powder sample (in wt%).

Sample ID	Fe	Cr	Yttrium	Titanium
P0	Bal.	14.5	0	0
P005	Bal.	14.5	0.06	0.08
P03	Bal.	14.5	0.16	0.22
P1	Bal.	14.5	0.65	0.91

3. Results

3.1. In situ synchrotron XRD

Identical non-isothermal heating cycles were performed from room temperature to 1100 °C on the four milled powders. Dislocation density and crystallite size were determined all along the cycles.

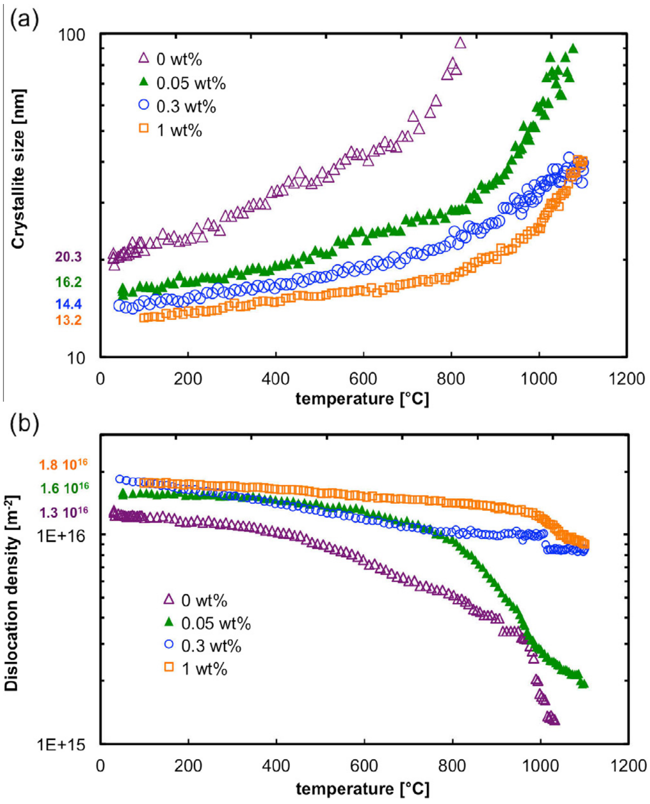

Fig. 1. Evolution of crystallite size upon non-isothermal heating up to 1100 °C (1373 K).

Fig. 1 reports the evolution of the crystallite size and the dislocation density for the four grades during annealing. The upper limit of detectable crystallite size was set at 100 nm, which corresponds to the resolution limit of the experimental set up. The initial crystallite size is 20.3 nm for the unreinforced grade whereas it slightly decreases with the amount of yttrium and titanium, which tends to prove that increasing the amount of oxide forming solutes refines the microstructure during mechanical alloying [22]. Mechanical alloying of ODS steels involves the milling of one ductile metallic phase with a brittle oxide. During intensive milling of this kind of system, the ductile powder particles get work hardened and their grain structures is refined [23]. The alloying process intensifies the lattice distortions by adding large solute elements (Y, Ti) at substitutional positions and oxygen atoms at interstitial sites, which can promote the build-up of a large dislocation density by reducing the level of dynamic recovery. This phenomenon is evidenced by the detection of a higher dislocation density for the most reinforced powder P1 ($\sim 1.8 \cdot 10^{16}\ \mathrm{m}^{-2}$) compared to the un-reinforced powder P0 ($\sim 1.3 \cdot 10^{16}\ \mathrm{m}^{-2}$) (Fig. 1(b)).

During the first stage of annealing, the crystallite size of the four different powders slowly increases with temperature. This increase in crystallite size is most likely due to recovery combined with grain growth. Evidence of recovery is given by the continuous decrease in the dislocation density of the four powders (Fig. 1(b)). During this stage, the crystallite growth rate is significantly higher for the P0 powder than for the others. This difference can be attributed to the solute drag effect on grain boundaries, which is efficient at low temperature [24–26]. Indeed, the mobility of the grain boundaries is lowered by the presence of solute segregation, which increases with the amount of yttrium and titanium in the powders. This effect is clearly identified as Fig. 1(b) shows that the higher the solute content, the lower the growth rate.

From 700 to 800 °C, two different behaviors are observed. First, the P0 and P005 powders undergo a decrease in the dislocation density slightly preceding a drastic increase in the crystallite size. These evolutions of both dislocation density and crystallite size are characteristic of the occurrence of recrystallization (cf. Ref. [20]). Thus, the P0 crystallite size rapidly reaches 100 nm at 850 °C whereas the P005 powder reaches the same size only at 1000 °C. From this temperature, one has to separately analyse each powder. Indeed, for P0 and P005 powders, the dislocation density completely drops and decreases down to respectively $10^{13}\ \mathrm{m}^{-2}$ and $5 \times 10^{13}\ \mathrm{m}^{-2}$. For the P03 and P1 powders, the problem is slightly different since the recrystallization within those powders is still not complete, the dislocation density can therefore still be very high in some of the crystallites while quite low in others. Furthermore, the measurement method used here is no longer suited to measure dislocation density after abnormal grain growth and the values given after this point must be taken with all the precaution due. Even if the XRD peak-broadening method intrinsically focuses on the small and deformed crystallites responsible for diffraction peak broadening, the appearance of larger recrystallized grains is clearly evidenced here. Namely, the drastic drop in dislocation density around 750 °C and 950 °C for P0 and P005 respectively associated with a large increase in grain size are evidences of abnormal grain growth. An illustration of abnormal grain growth is the significant growth rate difference between the mWH and the mWA–mWH methods [20], as highlighted in Supplementary material (online figure).

On the other side, the P03 and P1 powders experience only a limited evolution of the rate of increase of both dislocation density and crystallite size with increasing temperature. In average, the crystallite size increases to reach 40–50 nm in diameter and somehow stagnates at high temperature. This slight increase of crystallite size is accompanied by a limited but brutal decrease of the dislocation density, indicating a partial recrystallization at 950 °C.

To conclude on these results, we observe that the recrystallization temperature rises as yttrium and titanium content in the powder increases. More importantly, the extent of recrystallization is also limited by the solute content. Thus, the rapid growth of recrystallized grains induces much larger crystallite sizes in the least reinforced powders P0 and P005 compared to P03 and P1. In this context, increasing the solute content can be an efficient approach to avoid the appearance of abnormal grains during high-temperature consolidation. In order to quantify the effect of solute content on recrystallization and abnormal growth, *ex situ* examination was performed on the annealed powders.

3.2. Microstructure characterization after in situ annealing

After annealing, the powders were characterized by FEG-SEM. The microstructures obtained are reported in Fig. 2. The yttrium oxides having been identified as the main cause for abnormal grain growth [10,11], the grain structure was not expected to be bi-modal in P0. Yet, a bimodal microstructure with both ultrafine grains (submicron) and coarse grains was observed on the four powders. This is why direct observations (even limited to small probed volumes) are necessary to complete indirect XRD study, especially for highly heterogeneous microstructures. Nonetheless, the fraction of ultrafine grains clearly increases with the solute content while the mean size of ultrafine grains decreases. The Y–Ti free powder P0 contains a majority of coarse grains with a radius of 5–15 μm. Even its finest grains are quite large, with a diameter ranging from 0.5 to few microns. The latter are visibly pinned by particles at boundaries, with a high proportion of multiple junction sites occupied by precipitates, which in this powder are coarse oxides enriched in aluminum/chromium or carbides. The bi-modal microstructure evidenced in each powder can be related to the presence of particles in all powders and their particular position at multiple junction sites [10]. Theses precipitates vary in nature and size depending on the powder. On the P005 powder the surface fraction of abnormal grains is observed to be already much smaller than that in the P0 powder. The finest grains are also drastically smaller, with a mean radius below 0.2 μm. Interestingly when the content of yttrium and titanium is further increased to 0.3 wt% (P03 powder), the microstructure still exhibits some coarse grains even if they are mainly concentrated close to the surface of the powder particles. The surface fraction of ultra-fine grains is larger and shows a smaller mean size than those in the two powders P0 and P005, which confirms the important role of solute content on this population. Similarly, the powder P1 shows limited number of abnormal grains, mainly located on the powder particles edges. These complementary SEM observations are consistent with results from *in situ* X-ray diffraction. They confirm the appearance of abnormal microstructures in the powders. They also confirm that the extent of recrystallization and abnormal grain growth is very limited for the most reinforced powders. It is interesting to note that whatever the solute content, the abnormal grains always have the same size.

The size of UFGs in the P03 and P1 powders is below 100 nm, thus its quantification requires Transmission Electron Microscopy. A TEM–ACOM analysis was performed on each annealed powder, as reported in Fig. 3. This analysis confirmed the drastic decrease of the ultrafine grain radius with the solute content. The least reinforced grade contains only few fine grains below 1 μm. A significant decrease in UFG size between P0 and P005 is observed, demonstrating the benefit of adding, yttrium and titanium to form precipitates in the matrix that efficiently retain grain boundaries migration. P03 and P1 have finer UFG size than P005, indicating that the critical grain size can be tailored by the amount of the precipitating solutes.

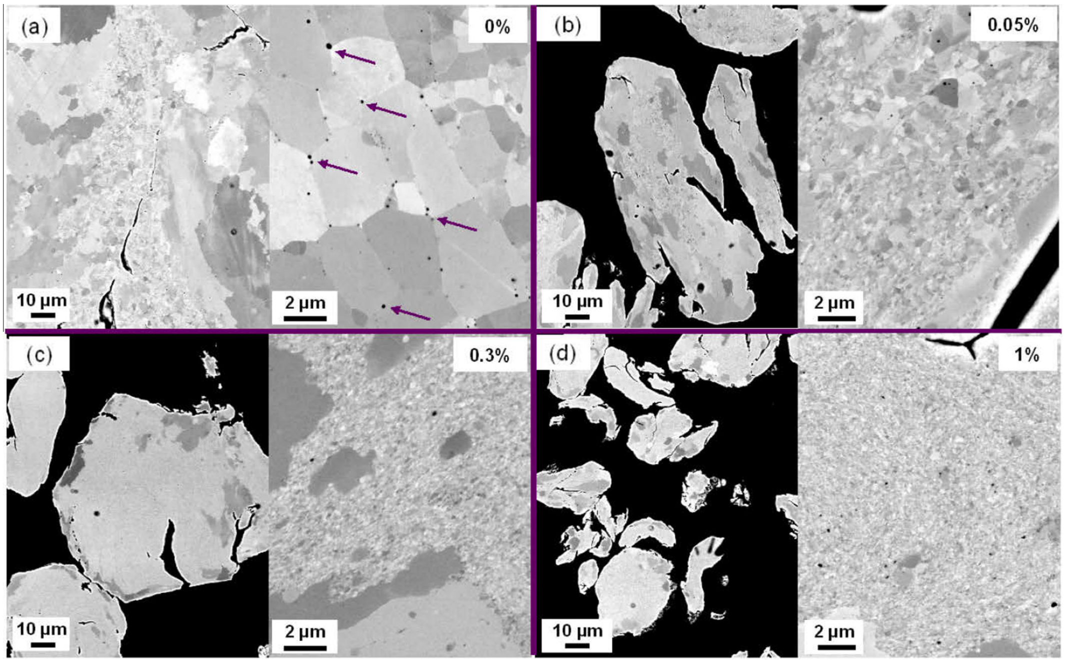

Fig. 2. SEM images of the microstructures of annealed powders: (a) P0, (b) P005, (c) P03 and (d) P1. Arrows indicate coarse oxides enriched in aluminum and titanium at (triple) grain boundaries. Other black dots that can be seen in the other three powders (b–d) are titanium oxides.

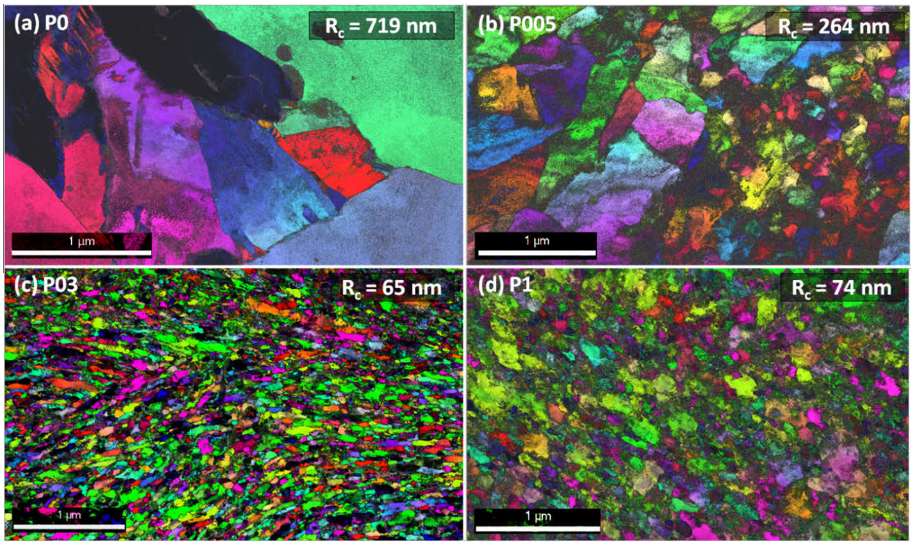

Fig. 3. TEM–ACOM orientation maps of each annealed powder (a–d). The mean grain radius for each sample is also reported.

There is no significant difference in UFG size between the P03 and P1 powders. However, the grain size measured in the P1 powder is probably overestimated. Indeed, in this powder, TEM–ACOM mapping is made more difficult by the very dense nanoprecipitation and the very important overlapping between different grains within the thickness of the FIB sample. This induces a strong disturbance on recorded diffraction patterns, which are composed of diffraction corresponding to multiple orientations. Thus, the orientation map in this sample is not as well resolved as the other maps (Fig. 4(d)).

3.3. Precipitation state in the consolidated/annealed materials

The heating cycle performed during the *in situ* synchrotron XRD experiment is representative of typical consolidation with hot isostatic pressing (HIP): a non-isothermal treatment from room temperature to around 1100 °C with an average heating rate of 30 °C min^{-1} followed by a 20 min annealing at 1100 °C and a slow cooling. The microstructure of the annealed powders and HIPed ODS steels are thus expected to be equivalent both in term of grain size and precipitation state. This is shown in Fig. 4 where the microstructures of the P03 powder HIPed at 1100 °C and the same P03 powder annealed during the *in situ* synchrotron experiment are compared.

Both microstructures show a bimodal microstructure with coarse grains and UFG with roughly the same fraction. Moreover, the precipitation state was measured on the four different powders processed by HIP at 1100 °C. The characterization was done using SAXS; a detailed presentation of SAXS data treating would fall out of the scope of the present paper and readers are reported to

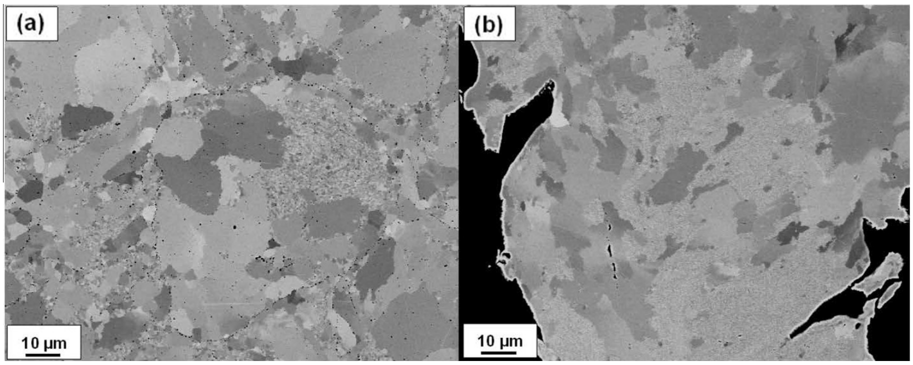

Fig. 4. SEM-FEG image (backscattered electrons) of: (a) the powder P03 processed by HIP at 1100 °C and (b) the powder P03 after annealing at 1100 °C at the synchrotron. Both have a bimodal microstructure.

[27]. However, one example of TEM observation performed on the HIPed P03 powder is presented in Fig. 5.

The precipitates are mostly cubic, with a radius of about 1–2 nm. Based on their particular structure factor contrast, precipitates are coherent or semi-coherent [28]. The precipitates fraction and mean radius measured on each HIPed powder by SAXS are summarized in Table 2. As expected, the volume fraction increases with the initial titanium and yttrium content, from 0.09% to 1.9% for the most reinforced grade (Table 2). The average radius of the few particles detected in the P0 powder is 3 nm, whereas the average radius in the three other powders is approximately 1 nm. This is consistent with the presence of coarser oxides or carbides in P0 while fine Y–Ti–O particles are expected in the three reinforced powders (P005, P03 and P1). Indeed, nanoscale characterization using Transmission Electron Microscopy and Atom-Probe Tomography performed in materials of same composition and equivalent processing conditions [4,29] showed that these particles were mainly ternary Y–Ti oxides.

During milling, yttrium and titanium atoms are dissolved in the matrix. Whether they form solid solution or amorphous subnanometric fragments is discussed in recent literature [30].

Since titanium and yttrium have low solubility in iron, the driving force for the precipitation of titanium and yttrium oxides in the matrix is very high. Given that the precipitation is a diffusion-activated mechanism, we assume that they form only during the high-temperature process.

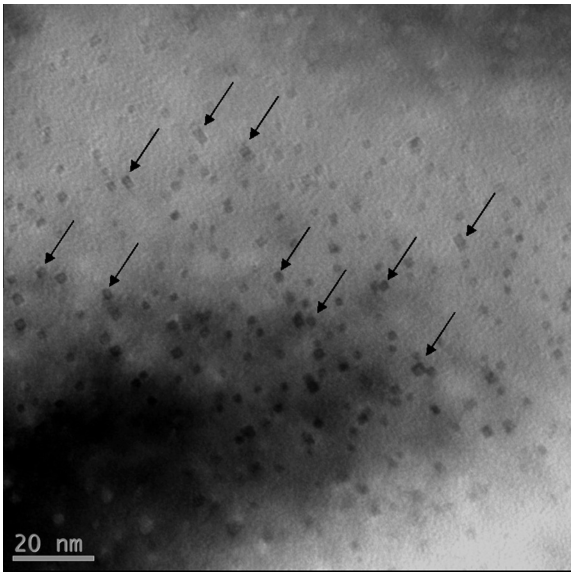

Fig. 5. TEM bright field image of nanosized oxides in very high density in the HIPed P03 powder.

Table 2
Precipitation state from SAXS experiments and resulting Zener pinning pressure for each HIPed sample with a grain boundary energy assumed to be $\gamma = 0.5\ \mathrm{J\ m^{-2}}$.

Sample	Mean radius (nm, SAXS)	Volume fraction (%, SAXS)	Volume fraction (%, theoretical)	Zener pinning pressure (MPa)
HIP-P0	3.0	0.19	0.007	0.5
HIP-P005	1.1	0.35	0.2	2.4
HIP-P03	1.3	0.72	0.55	4.2
HIP-P1	0.9	1.9	2.22	15.6

Considering yttrium as to limiting element, the theoretical volume fraction of ternary oxides $Y_2Ti_2O_7$ is lower than that determined by SAXS (Table 2), except for HIP-P1. This means that yttrium is most likely completely in the oxides. This also means that other solutes, such as aluminum and chromium can take part to the composition of the nanosized particles, as emphasized by Atom-Probe Tomography [31]. Nevertheless, this slight discrepancy between SAXS and theoretical oxides fraction can have multiple sources. One of the most important is that the precipitation state includes different populations of oxides ($Y_2Ti_2O_7$, Y_2O_3, $Y_2Ti_2O_5$).

The direct relationship between the precipitate density and the initial solute content of yttrium and titanium is particularly interesting to design the microstructure. Indeed, the Zener pining pressure P_Z in the reinforced powders can be more easily tailored by the precipitation fraction at constant mean radius.

$$P_Z = \frac{3}{2}\gamma\frac{f_p}{r_p}$$

where γ is the grain boundary energy, f_p and r_p the fraction and mean radius of the precipitates. Values of pinning pressures exerted by particles on grain boundaries are given in Table 2.

4. Discussion

(a) Size of ultrafine grains

One particularly interesting property of ODS steels is the extreme thermal stability of ultrafine grains. Indeed, UFGs provide Hall–Petch strengthening and are therefore of key interest. Especially, they are very stable under thermal treatment at high temperature. We propose here to explain the evolution of this population of grains as a function of yttrium and titanium content and therefore as a function of its interaction with nanosized particles. The competition between the driving pressure for grain growth against the retarding pressure can be translated into the following equation:

$$\sum P_i = P_C - P_Z = \gamma\left(\frac{2}{R} - \frac{3f_p}{2r_p}\right) = 0$$

where P_C is the capillary pressure governed by the grain boundary curvature effect and P_Z is the Zener pinning pressure due to precipitates at grain boundaries. We consider here that the stored energy is homogeneous between UFGs and therefore does not provides any additional driving force for grain boundary migration. This equation allows to derive the critical size reached by UFG when the Zener pinning pressure and driving pressure are equal:

$$R_C^{\text{Zener}} = 4r_p/3f_P$$

It is worth noticing that Rios modified the Zener theory, resulting in a critical grain size 8 times smaller [32]:

$$R_C^{\text{Rios}} = r_p/6f_P$$

The critical size of ultrafine grains was calculated using the Small-Angle X-ray Scattering (SAXS) data on the four powders consolidated by Hot Isostatic Pressing at 1100 °C (cf. Table 2). A consistent match between calculated and effectively measured UFG size is obtained for the different alloys (Fig. 6). Given the experimental errors, the measured radius of the ultrafine grains is well predicted by the theory of competing pressures and is included between the two values predicted by Zener and Rios for each yttrium and titanium content. Specifically, the size of the ultrafine grains follows, for investigated range of solute content, the criterion:

$$R_C^{\text{ODS}} = 0.71\ r_p/f_p$$

When dealing with low fraction of second-phase particles, the more efficient pinning by particles located at multiple grain junctions is most likely responsible for reducing the grain size [10]. However, the calculated critical size of the ultrafine grains accurately matches the UFG size measured by TEM. As mentioned before, the measured grain size of the P1 powder can be overestimated by TEM–ACOM because of the amount of distortions present in this material and the overlapping of grains within the thickness of the sample. However, this can also results from a saturation effect. If every grain boundary is covered with precipitates, adding more precipitates will not result in a stronger pinning effect. The Zener formulae clearly does not take this possibility into account and given the very high precipitate density in the P1 sample, this situation may arise.

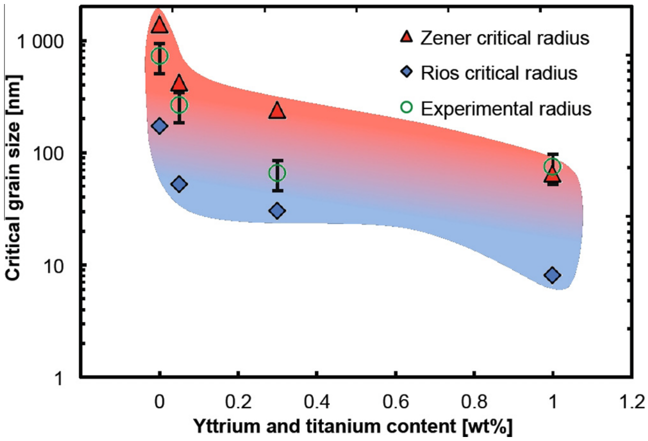

Fig. 6. Critical size calculated from Zener and Rios theories based on the precipitation state determined on each grade. Experimental measurements of ultrafine grains (UFG) size were performed by TEM–ACOM.

(b) Bimodal microstructure

The second relevant result that needs to be discussed is the appearance of the bimodal microstructure whatever the titanium and yttrium content. Consequently, it seems that this phenomenon is not entirely governed by the precipitation state, and it does not fit Zener theory based on the competition between pinning and capillary driving pressures. Since the plastic deformation on each powder during milling is drastic, it gives rise to a high level of stored energy. Differences in stored energy between neighboring grains directly translate in an additional driving pressure for grain growth called strain-induced boundary migration (SIBM). Following this mechanism, the grain boundaries move into the more deformed grains, resulting in the growth of the least deformed ones. The quantification of this driving pressure using experimental parameters in ODS steels was previously reported in [33]. It may result in either primary (nucleation of new grains) or continuous recrystallization (polygonization of former grains) followed by secondary recrystallization (abnormal growth of existing grains). This driving pressure combined with the capillary driving pressure P_C will compete with the pinning pressure from the precipitates. Therefore, the formation and further growth of the abnormal grains will be also affected by the state of precipitation. This mechanism is clearly emphasized by the increase of the recrystallization temperature with titanium and yttrium content. The full characterization of second-phase particles would be extremely interesting and allow, for example, to determine if normal and abnormal grain can be distinguished in terms of precipitate density.

5. Conclusion

In order to quantify the effect of the precipitation on the microstructure of ODS ultrafine grained ferritic steels, four powders were milled with different amounts of titanium, yttrium and oxygen. Using synchrotron X-ray diffraction with *in situ* annealing, a coupled modified Warren–Averbach and Williamson–Hall method was applied to determine the crystallite size and dislocation density during heating. A focus was made on the evolution of ultrafine grains, which are known to harden the metallic materials. Specially, the powders annealed in the synchrotron were characterized by TEM–ACOM. The size of ultrafine grains was determined and compared to the critical grain size predicted by Zener original and modified theory, calculated from the precipitation state (mean radius and volume fraction) measured by Small-Angle X-ray Scattering (SAXS).

- Concerning the as-milled powder before heating, the dislocation density of more than $10^{16}\ \text{m}^{-2}$ is representative of the intense plastic deformation experienced during milling. It is observed to increase with the amount of titanium and yttrium.
- Abnormal growth during heating is observed for every powder. Our results suggest that the heterogeneity of the milled powder, particularly in terms of plastic stored energy, is mainly responsible for the formation of abnormal grains and their growth at the expense of the ultra fine grains (UFG).
- Increasing the content of titanium and yttrium increases the volume fraction of precipitates and therefore the Zener pinning pressure on grain boundaries. This induces an increase in the temperature above which abnormal growth occurs. If this temperature is higher than that necessary to consolidate the powder, abnormal growth may be avoided and a homogeneous

and ultrafine microstructure could be obtained. Also, increasing the solute content gives rise to an increase of the ratio between ultrafine and coarse grains and a decrease in the size of the UFG. The critical grain size of ultrafine grained ODS steel responds to the following criterion:

$$\begin{cases} R_C^{\mathrm{ODS}} = C^{\mathrm{ODS}}\, r_p/f_p \\ C^{\mathrm{Zener}} = 4/3 \leqslant C^{\mathrm{ODS}} \approx 0.71 \leqslant C^{\mathrm{Rios}} = 1/6 \end{cases}$$

Since the fraction and the size of the UFG in bimodally structured metallic materials is a key parameter that controls the mechanical properties [12,13,34], this comprehensive relationship between the solute content and the UFG could be applied to tailor the mechanical properties of ODS ferritic steels.

Acknowledgments

X. Boulnat was supported by the European Community within the FP7 Project MATTER and in the frame of a tripartite agreement between the CEA, AREVA and EDF. N. Sallez was supported by the joint program “CPR ODISSEE” funded by Areva, CEA, CNRS, EDF and Mécachrome under contract No. 070551. The staff of the DIFFABS beamline at SOLEIL is warmly acknowledged. This work was carried out with the partial support of the Karlsruhe Nano Micro Facility (KNMF, www.kit.edu/knmf), a Helmholtz Research Infrastructure at Karlsruhe Institute of Technology.

Appendix A. Supplementary data

Supplementary data associated with this article can be found, in the online version, at http://dx.doi.org/10.1016/j.actamat.2015.07.005.

References

[1] P. Dubuisson, Y. de Carlan, V. Garat, M. Blat, J. Nucl. Mater. 428 (2012) 6.
[2] P. Miao, G.R. Odette, T. Yamamoto, M. Alinger, D. Hoelzer, D. Gragg, J. Nucl. Mater. 367–370 (Part A) (2007) 208.
[3] M.J. Alinger, G.R. Odette, D.T. Hoelzer, Acta Mater. 57 (2009) 392.
[4] C.A. Williams, P. Unifantowicz, N. Baluc, G.D.W. Smith, E.A. Marquis, Acta Mater. 61 (2013) 2219.
[5] B. Fournier, A. Steckmeyer, A.-L. Rouffie, J. Malaplate, J. Garnier, M. Ratti, P. Wident, L. Ziolek, I. Tournie, V. Rabeau, J.M. Gentzbittel, T. Kruml, I. Kubena, J. Nucl. Mater. 430 (2012) 142.
[6] C. Heintze, F. Bergner, A. Ulbricht, M. Hernández-Mayoral, U. Keiderling, R. Lindau, T. Weissgärber, J. Nucl. Mater. 416 (2011) 35.
[7] X. Boulnat, D. Fabregue, M. Perez, M.-H. Mathon, Y. de Carlan, Metall. Mater. Trans. A 44 (2013) 2461.
[8] M. Hillert, Acta Metall. 13 (1965) 227.
[9] T. Gladman, Scr. Metall. Mater. 27 (1992) 1569.
[10] Y. Bréchet, M. Militzer, Scr. Mater. 52 (2005) 1299.
[11] V.Y. Novikov, Mater. Lett. 84 (2012) 136.
[12] Z. Dapeng, L. Yong, L. Feng, W. Yuren, Z. Liujie, D. Yuhai, Mater. Lett. 65 (2011) 1672.
[13] Y. Wen, Y. Liu, A. Hirata, F. Liu, T. Fujita, Y. Dou, D. Liu, B. Liu, Z. Liu, C.T. Liu, Mater. Sci. Eng., A 544 (2012) 59.
[14] T. Ungar, A. Borbely, Appl. Phys. Lett. 69 (1996) 3173.
[15] T. Ungár, I. Dragomir, A. Révész, A. Borbély, J. Appl. Crystallogr. 32 (1999) 992.
[16] T. Shintani, Y. Murata, Acta Mater. 59 (2011) 4314.
[17] R.A. Renzetti, H.R.Z. Sandim, R.E. Bolmaro, P.A. Suzuki, A. Möslang, Mater. Sci. Eng., A 534 (2012) 142.
[18] E. Lauridsen, D.J. Jensen, H. Poulsen, U. Lienert, Scr. Mater. 43 (2000) 561.
[19] S. Malinov, W. Sha, Z. Guo, C.C. Tang, A.E. Long, Mater. Charact. 48 (2002) 279.
[20] N. Sallez, X. Boulnat, A. Borbély, J.L. Béchade, D. Fabrègue, M. Perez, Y. de Carlan, L. Hennet, C. Mocuta, D. Thiaudière, Y. Bréchet, Acta Mater. 87 (2015) 377.
[21] C. Le Bourlot, P. Landois, S. Djaziri, P.-O. Renault, E. Le Bourhis, P. Goudeau, M. Pinault, M. Mayne-L’Hermite, B. Bacroix, D. Faurie, O. Castelnau, P. Launois, S. Rouzière, J. Appl. Crystallogr. 45 (2012) 38.
[22] J.M. Torralba, L. Fuentes-Pacheco, N. García-Rodríguez, M. Campos, Adv. Powder Technol. 24 (2013) 813.
[23] C. Suryanarayana, Prog. Mater. Sci. 46 (2001) 1.
[24] J.W. Cahn, Acta Metall. 10 (1962) 789.
[25] K. Lücke, H.P. Stüwe, Acta Metall. 19 (1971) 1087.
[26] M. Hillert, B. Sundman, Acta Metall. 24 (1976) 731.
[27] F. De Geuser, A. Deschamps, Comptes Rendus Phys. 13 (2012) 246.
[28] M.F. Ashby, L.M. Brown, Philos. Mag. 8 (1963) 1649.
[29] J. Ribis, Y. de Carlan, Acta Mater. 60 (2012) 238.
[30] I. Hilger, M. Tegel, M.J. Gorley, P.S. Grant, T. Weißgärber, B. Kieback, J. Nucl. Mater. 447 (2014) 242.
[31] V. De Castro, E.A. Marquis, S. Lozano-Perez, R. Pareja, M.L. Jenkins, Acta Mater. 59 (2011) 3927.
[32] P.R. Rios, Acta Metall. 35 (1987) 2805.
[33] X. Boulnat, M. Perez, D. Fabrègue, T. Douillard, M.-H. Mathon, Y. de Carlan, Metall. Mater. Trans. A 45 (2014) 1485.
[34] B. Mouawad, X. Boulnat, D. Fabrègue, M. Perez, Y. de Carlan, J. Nucl. Mater. 465 (2015) 54.